



Cite this: *Nanoscale*, 2019, **11**, 18702

Assembly by solvent evaporation: equilibrium structures and relaxation times†

Tommy Waltmann and Alex Travesset *

We present a study describing the dynamics and equilibrium of the assembly of nanostructures by solvent evaporation. We first consider N nanocrystals stabilized by capping ligands in a spherical droplet of liquid solvent coexisting with its gas and show that, as the liquid solvent evaporates slowly, NCs crystallize into clusters of high symmetry based on tetrahedral and octahedral units: tetrahedron ($N = 4$), octahedron ($N = 6$), icosahedron ($N = 13$), Archimedean truncated tetrahedron ($N = 16$) and Z_{20} ($N = 21$). We derive explicit formulas for the process and rigorously compute relaxation times, which drastically increase when the packing parameter reaches the hard-sphere liquid–solid transition $\eta_{HS}^f = 0.49$. This result shows that contrary to what occurs in an evaporation of a single component system, the relaxation times are not determined by the diffusion constant of the vapor, but rather, are dominated by the residence time of solvent molecules trapped within the capping ligands. Our theory provides a number of predictions that enable the design of new structures while improving the control and quality of their assembly.

Received 11th July 2019,
 Accepted 30th September 2019
 DOI: 10.1039/c9nr05908c
rsc.li/nanoscale

Introduction

Assembly of nanocrystals (NCs) into structures with long range order, *i.e.* superlattices (SLs), is a fundamental practical problem with far-reaching implications in many critical fields.¹ Over the last decade, many strategies have been developed for synthesizing single component and binary SLs (BNSLs) such as DNA assembly,^{2–4} electrostatic regulation⁵ or interpolymer complexation.⁶ Another very successful strategy is solvent evaporation (SE),⁷ which has lead to a myriad of intricate BNSLs and quasicrystals with fascinating order.^{1,8,9}

A typical SE experiment consists of NCs stabilized by capping ligands of saturated or unsaturated hydrocarbons in an organic solvent, such as decane or toluene, that are gradually evaporated until the NCs crystallize.⁸ While almost all experimental methods have relied on SL crystallization on a substrate (*i.e.* heterogeneous nucleation),¹ recently, Wang *et al.*¹⁰ and Yang *et al.*¹¹ have devised new methods consisting

of encapsulating NCs in oil droplets, thus synthesizing single component and BNSLs through homogeneous nucleation, obtaining the same structures as in heterogeneous nucleation, thus providing very strong evidence that BNSLs are indeed true equilibrium structures. Other experiments^{12,13} have investigated the structure of clusters that emerge when the quality of the solvent is tuned (ST) in stable NC suspensions. Still, despite the enormous success of SE, many fundamental questions are still unresolved, such as how much solvent (if any) remains in the final equilibrium structure, how the parameters controlling the evaporation process affect the quality of the final SLs, or the sequence of events and potential barriers that lead to crystallization. This includes identification of intermediate structures, such as an fcc to bcc (Bain)^{14,15} or hcp to bcc¹⁶ transition. Furthermore, it is well known¹ that SE and ST do not generally result in the same structures for the same conditions, raising issues related to metastability. The goal of this paper is to provide a microscopic description of SE that will lead to a conclusive answer to all of these very fundamental questions.

There are very few theoretical studies of assembly by SE, though many authors have investigated models where the solvent is considered implicitly.^{17,18} Particularly relevant is the recent study by Fan and Grünwald,¹⁵ who have characterized the different types of orientational order during NC self-assembly. There are even less studies with explicit solvent, one by Cheng and Grest^{19,20} and another by Howard *et al.*,²¹ who have performed a large scale MD simulation consisting

Department of Physics & Astronomy and Ames Laboratory – USDOE,
 Iowa State University, Ames, IA 50011, USA. E-mail: trvss@ameslab.gov

† Electronic supplementary information (ESI) available: Definition of droplet radius (R_d); additional results for pure toluene; dependence of the droplet radius R_d on ρ_{avg} ; additional results for solvent evaporation with $N = 2, 4, 6, 13, 16, 21$; dependence of the NN distance on the droplet packing fraction η_{HS} ; complementary results for the free energy. See DOI: [10.1039/C9NR05908C](https://doi.org/10.1039/C9NR05908C)



of Lennard-Jones particles at the liquid/gas coexistence with hard-sphere colloidal particles, reaching the interesting conclusion that the final crystal structure does not depend significantly on the evaporation rate, as the initial surface structure formed at the interface is subsequently deformed due to confinement effects. In all these studies, the Peclet (Pe) number has been shown to be a relevant parameter characterizing the quality of the assembly.²² The Pe number is defined as:

$$\text{Pe} = \frac{Hv}{D}, \quad (1)$$

where H is the initial size of the film, v the velocity of the growing interface and D is the diffusion constant. Intuitively, for $\text{Pe} \ll 1$ the diffusion is sufficiently fast and good crystallization becomes possible, while for $\text{Pe} \gg 1$, the crystal “breaks” into small domains likely not well equilibrated.

In this paper, we present a microscopic description for assembly of NCs through SE. Some of the considerations discussed above still apply in a coarse-grained sense, that is, when NC are modeled as effective hard sphere (HS) or Lennard-Jones particles.^{23,24} Yet, in previous papers we have shown the limitations of these coarse grained approaches, as NCs within nanostructures bond through certain ligand configurations (“vortices”) that cannot be accounted by these simpler models, and are determined by the “Orbifold Topological Model” (OTM)^{25,26} instead. It is also intuitive that the interaction of the capping ligands with the solvent does play a non-trivial role. Hence, it is necessary to consider models where the ligands and their interaction with solvent are included explicitly.

Results

Simulations used HOOMD-Blue^{27,28} with the OPLS/united force field²⁹ as implemented in HOODLT.³⁰ The parameters for toluene were obtained from ref. 31. We ran simulations within the NVT ensemble. Liquid and gas phases are identified according to the Voronoi construction as described in ref. 32 and 33. The experimental data for toluene was taken from ref. 34.

We prepare a simulation by placing a number N_t of solvent (toluene) particles in a box of volume V . The average (or nominal) density is defined as:

$$\rho_{\text{avg}} = M_w \frac{N_t}{V}, \quad (2)$$

where $M_w = 0.09214 \text{ kg mol}^{-1}$ and N_t/V is expressed in mol m^{-3} . Often in this paper, the solvent phase separates into a liquid and gas with respective densities ρ_l , ρ_g , so ρ_{avg} does not generally represent a physically realizable density of an homogeneous system.

We place a number N of gold NCs functionalized with 80 dodecane molecules through a thiol bond ($\text{Au}_{201}(\text{SC}_{12})_{80}$). The core radius is $R_{\text{core}} = 10.15 \text{ \AA}$ and the grafting density $\sigma = 0.595$

chains per \AA^2 . The hard sphere radius of the NC is given by the OPM formula:^{26,35}

$$R_{\text{HS}} = R_{\text{core}} \tau_{\text{OPM}} = R_{\text{core}} (1 + 3\lambda\xi)^{1/3} = 17.9 \text{ \AA}, \quad (3)$$

where $\lambda = L/R_{\text{core}}$ and $\xi = \sigma/\sigma_{\text{max}}$, with L the maximum extension of the ligands and σ_{max} the maximum grafting density. From previous studies,³⁶ $\sigma_{\text{max}} = 0.666$ chains per \AA^2 . Note that if R_d (to be precisely defined further below) is the radius of the liquid droplet, the hard sphere packing fraction is defined by:

$$\eta_{\text{HS}} = \frac{4\pi/3 N R_{\text{HS}}^3}{4\pi/3 R_d^3} = N \left(\frac{R_{\text{HS}}}{R_d} \right)^3. \quad (4)$$

Further details of the NCs have been discussed in, for example, ref. 37.

Pure toluene

Following our previous simulations^{37–39} we kept the temperature at $T = 387 \text{ K}$, where according to ref. 34, the toluene coexistence between liquid and gas occurs at a pressure $P_c(387 \text{ K}) = 1.097 \text{ atm}$, saturated densities $\rho_l = 777.9 \text{ kg m}^{-3}$ and $\rho_g = 3.3 \text{ kg m}^{-3}$, and isothermal compressibility $\kappa_T = 1.866 \times 10^{-4} \text{ atm}^{-1}$.

For visualization purposes, we define gas, liquid, and interface regions as follows: the gas cutoff is defined as $30\rho_g$, the liquid cutoff is defined as $0.75\rho_l$. Results do not change significantly with other values. Any toluene which has local density greater than $0.75\rho_l$ is defined as liquid, any toluene with local density less than $30\rho_g$ is defined as gas, and any toluene that is neither of those is defined as interface, see Fig. 1a and b.

The local solvent density is determined from the local solvent volume, which is computed by voronoi tessellation implemented in the Freud⁴⁰ analysis package, where each input point is the center of mass of a toluene molecule.

Similar plots including many other ρ_{avg} values are shown in Fig. S3.[†] The saturated liquid density, as obtained from the simulation is given at $\rho_l^s = 780(4) \text{ kg m}^{-3}$, which compares very well with the experimental result $\rho_l = 777.9 \text{ kg m}^{-3}$, quoted above.

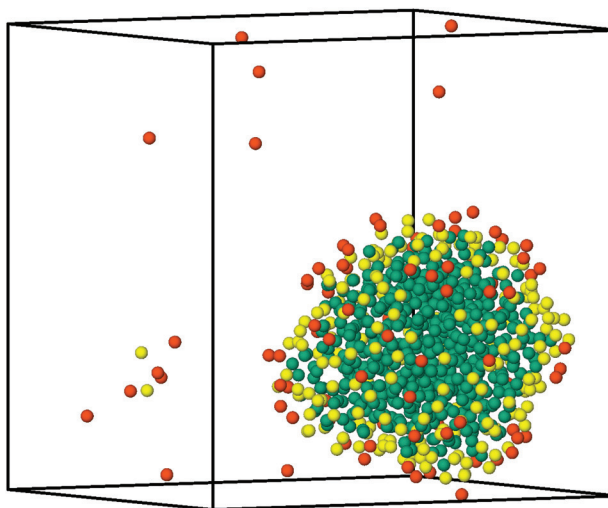
The histogram plots in Fig. 1b, provide an alternative way to determine the pressure when there is liquid–gas coexistence; with the gas density determined from the low density peak in Fig. 1b, a pressure is given by the ideal gas law:

$$P = \rho_g^s \frac{RT}{M_w}. \quad (5)$$

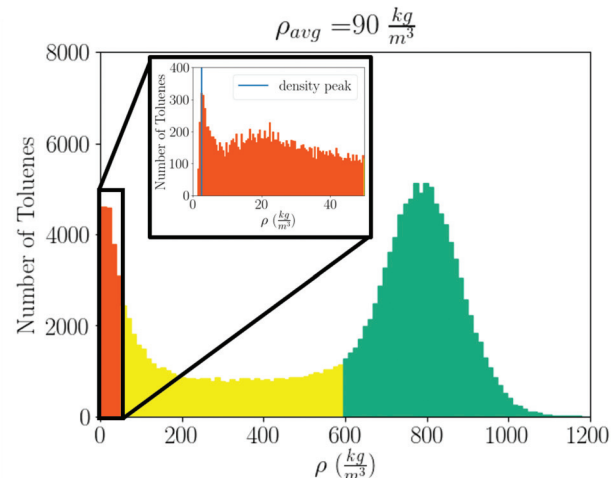
For example, from Fig. 1b one determines $P = 1.05 \text{ atm}$, which compares well with the experimental result for liquid–gas coexistence at this temperature $P_{\text{exp}} = 1.11 \text{ atm}$. A plot comparing the ideal gas pressure to that given by the simulation is shown in Fig. 2. We show in ESI, see Fig. S2,[†] that the pressure as it reads from the simulation becomes negative within the coexistence region, unlike eqn (5) that remains approximately constant, see Fig. S10.[†]

The process of solvent evaporation is illustrated in Fig. 3: the initial state consists of a liquid droplet in coexistence with





(a) Snapshot from the simulation



(b) Colored Local Density Histogram.

Fig. 1 (Left) Snapshot of a simulation with $\rho_{\text{avg}} = 90 \text{ kg m}^{-3}$ for toluene, along with its local density histogram (right). In (a), we use one particle to represent the entire toluene molecule, placed at its center of mass. Simultaneously in the box are particles in the liquid (green), vapor (orange), and interface (yellow) states. There are two yellow toluenes which may appear to be out of place, but they are in fact part of the interface because of boundary conditions.

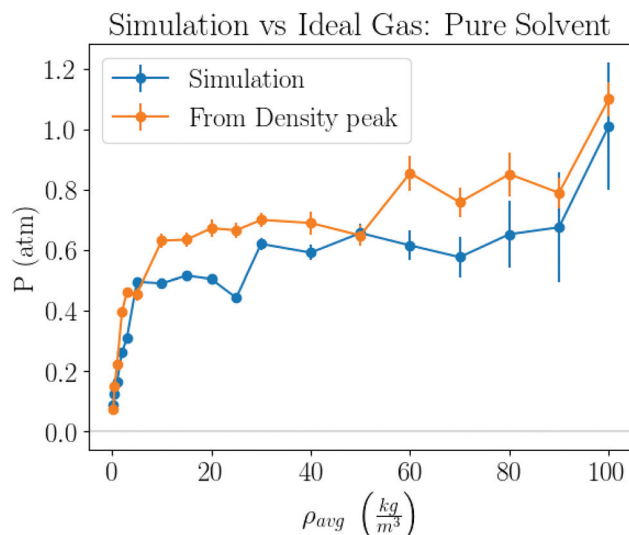


Fig. 2 Pressure obtained by 2 different methods. One method takes pressure data logged by the simulation, and the other computes the pressure from the peak in the gas density distribution, similar to the inset of Fig. 1b, and the ideal gas law, eqn (5).

the gas phase, which is slowly evaporated by expanding the simulation box until no liquid remains. Note that this is a different method than the one used in previous studies.²⁰ The liquid phase, see Fig. 1a, organizes into a spherical droplet. In Fig. 4a, we show the radius of the droplet as the solvent evaporates. The toluene density profile is computed by identifying the molecule at the center of the droplet and then calculating the radial distribution function using this molecule as our reference point. We accumulate this function over 200 frames

of our simulation (with all frames having the same box length and therefore the same ρ_{avg}). The plot for $\rho_{\text{avg}} = 10 \text{ kg m}^{-3}$ is shown in Fig. 4b. There are 3 clearly distinguished regions: $R < R_{\text{liquid}}$, $R_{\text{liquid}} < R < R_{\text{liquid+interface}}$, and $R_{\text{liquid+interface}} < R$. For $R < R_{\text{liquid}}$ the curve follows a typical radial liquid distribution function (rdf). Then at the interface region (where $R_{\text{liquid}} < R < R_{\text{liquid+interface}}$), there is a distinct transition in density from the saturated liquid density to the density of the vapor. The 3rd region $R_{\text{liquid+interface}} < R$ corresponds to the vapor. Hereon, the droplet radius is defined as $R_{\text{droplet}} = R_d = 0.825R_{\text{liquid+interface}}$, shown in Fig. 4a and b, so that it has the value as defined by the Gibbs interface, see the discussion in eqn (S4).†

Self-assembly of NCs

We now investigate assembly by SE for a toluene system in liquid/gas coexistence containing $N = 2, 4, 6, 13, 16$ and 21 NCs, so that the choices of N are basically random. Then the droplets are evaporated following the same protocol as in Fig. 3. Additional illustrations of the process are provided in ESI, see Fig. S5† and many others.

$N = 2$ (NC pair). The simplest case of SE is for a pair of $\text{Au}_{201}(\text{SC}_{12})_{80}$ NCs. The two NCs remain within the liquid droplet, with an equilibrium separation between the two NCs as a function of ρ_{avg} shown in Fig. 5a. Once the solvent is completely evaporated, the resulting equilibrium separation agrees with the minimum of the potential of mean force in vacuum, which has been reported in ref. 37. Note that the droplet radius and the NC separation curves are perfectly correlated.

Shown in Fig. 5c is the fraction of toluene molecules which are inside the interaction region between the 2 NCs. More precisely, the interaction region is divided into an ‘outer cone’, the OCM cone, defined by an angle $\phi_{\text{outer}} = \phi_{\text{OCM}}$ (see ref. 37),



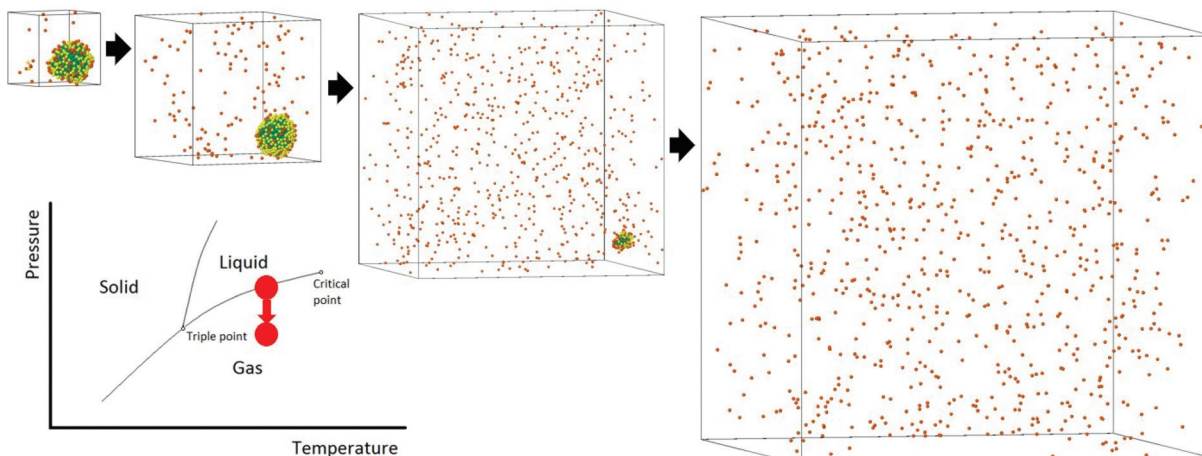


Fig. 3 The process of solvent evaporation. An initial liquid–gas at coexistence is run for a given amount of time after which the box is expanded. The process is repeated until all the solvent is found in the gas phase. After the last toluene molecule evaporates, the system moves away from the liquid–gas coexistence line.

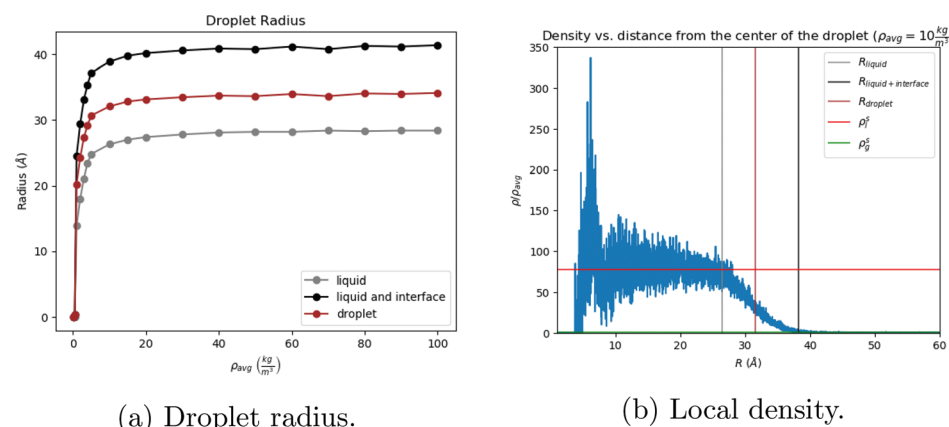


Fig. 4 (Left) Droplet radius: The gray curve comprises liquid particles only, the black includes the interface, and the brown is the droplet radius. (Right) Local density as a function of distance from the center of the liquid droplet. The plot follows a normal rdf at the saturated liquid density, then the density drops to that of the vapor. The vertical lines are data points taken directly from (a).

and an ‘inner cone’, in a manner similar to the OCM cone, where $\phi_{\text{inner}} = \phi_{\text{OCM}}/2$. From Fig. 5c, the inner cone is less densely packed with solvent molecules throughout the process of evaporation than the outer cone, reflecting the nature of the hydrocarbons to pack more densely in the inner cone than in the outer cone, noted in ref. 37. In addition, Fig. 5c shows that the solvent molecules are not expelled from the interaction region until the latest stages of solvent evaporation.

Vortices appear when solvent is almost evaporated. For our 3 lowest densities, $\rho_{\text{avg}} = 0.25, 0.5, 1.0$, the vortex textures shown in Fig. 6 appear at trace solvent. Even for $\rho_{\text{avg}} > 1.0 \text{ kg m}^{-3}$ the NCs separation is large enough that they do not form, see the right of Fig. 6.

N = 4. As the solvent evaporates the average inter-NC distance for each NC is shown below in Fig. 7b. At the end of the evaporation process, illustrated in Fig. 7c, the equilibrium configuration is a regular tetrahedron, see Fig. 9a.

N = 6. The equilibrium configuration after the solvent is evaporated is a regular octahedron, shown in Fig. 9b.

N = 13. Results for inter-NC distances are shown in Fig. 8a, resulting in an equilibrium NC assembly consisting of a regular icosahedron (depicted in Fig. 9c), that converges to the dry equilibrium separation reported in Ref. 39. Rather interestingly, as shown in Fig. 8b, the ratio between the edges, describing average center to vertex and vertex to vertex distances, match the ideal result for a perfect icosahedron

$$r = \sqrt{2 \left(1 - \frac{1}{\sqrt{5}}\right)},$$

showing that already in the liquid state, the NCs form a fluctuating icosahedron. As shown in Fig. 8c, the central NC in the icosahedron displays no vortices, in agreement with previous results³⁹ and the OTM.

N = 16. The equilibrium configuration for $N = 16$ after the solvent is evaporated is the Archimedean solid known as the truncated tetrahedra, shown in Fig. 9d.

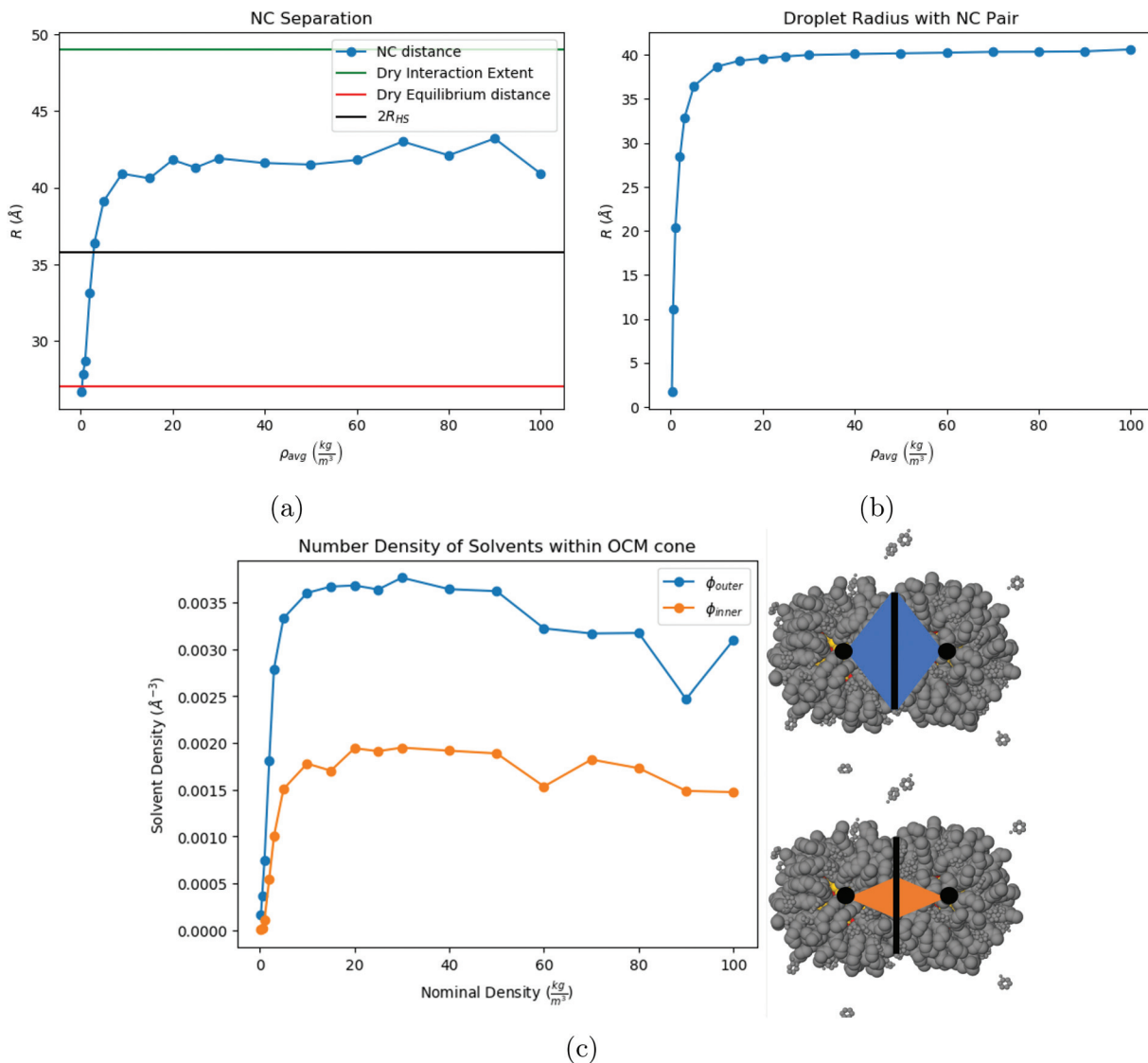


Fig. 5 Our results for a pair of NCs. (a) Shows a plot of the NC separation for $N = 2$ NCs. (b) Shows the radius of the droplet that contains the NCs. (c) Shows the number density of toluene molecules contained within the outer and inner OCM cone, along with a visual depiction of the two cones.

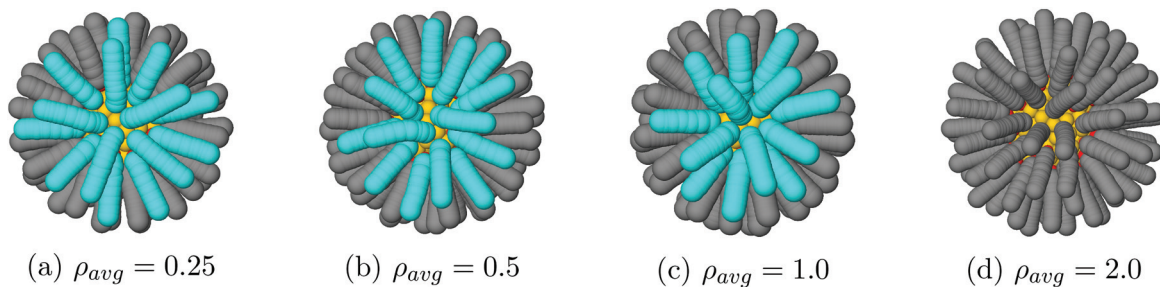


Fig. 6 Vortex texture formation for $N = 2$. No vortices are observed for any $\rho_{avg} > 1.0 \text{ kg m}^{-3}$.

$N = 21$. The equilibrium configuration for $N = 21$ after evaporating the solvent is shown in Fig. 9e. It is characterized by a northern hemisphere consisting of an hexagonal vertex at the north pole, a ring of six pentagonal

vertices and the same staggered configuration at the southern hemisphere. This polyhedra, labelled Z_{20} , was predicted as a constituent of Quasi-Frank-Kasper phases in ref. 41.

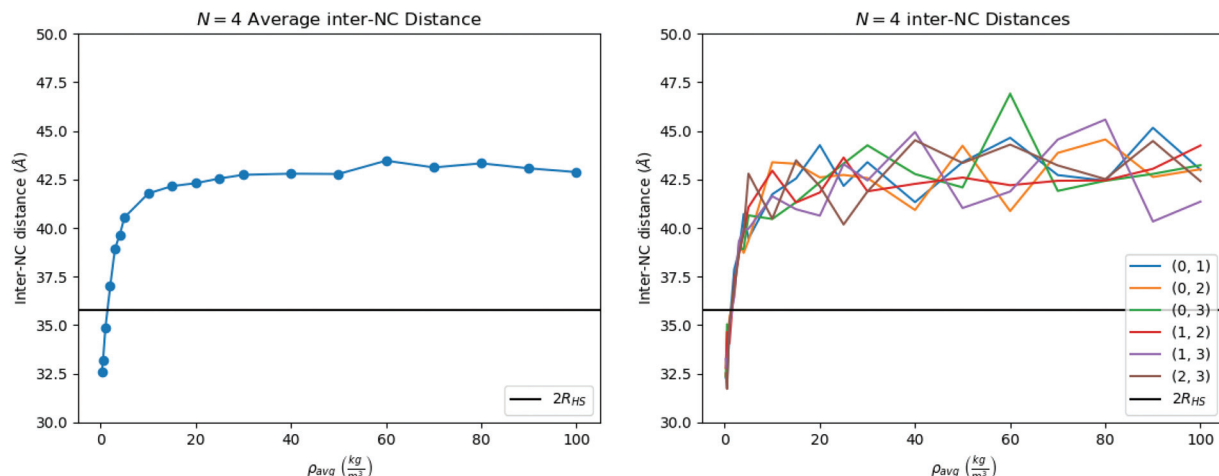


Fig. 7 Our results for $N = 4$ NPs. One can see that the system first assembles into a tetrahedron around $\rho_{\text{avg}} = 10 \text{ kg m}^{-3}$, shown in (b), and that once the solvent is fully evaporated, the equilibrium structure is indeed a tetrahedron, see Fig. 9a. The OPM value for the distance between 2 NPs is marked as a black line in both (a) and in (b).

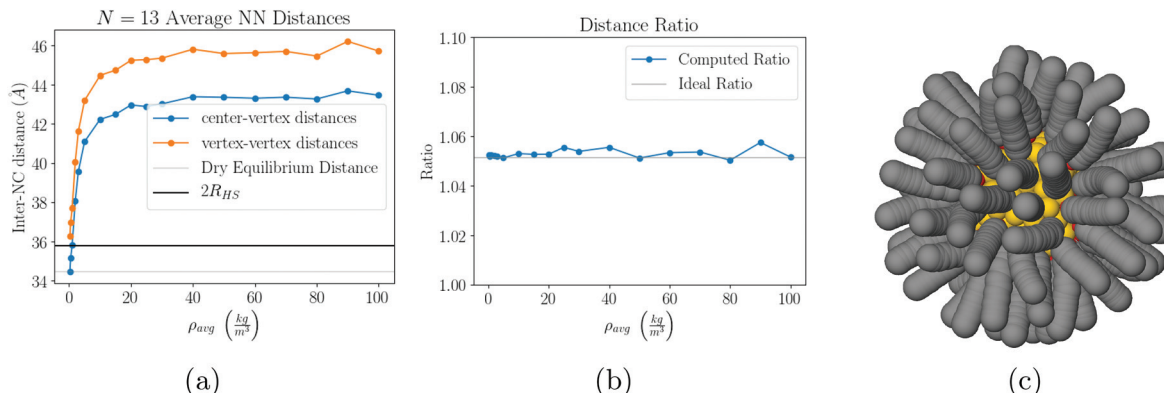


Fig. 8 Our results for $N = 13$. As the solvent evaporates, the system evolves into a symmetric configuration of 12 NCs in a cage and 1 NC trapped in the center, see (a) and (b). Once the solvent has completely evaporated, the equilibrium configuration is a perfect icosahedron (Fig. 9c), with the trapped NC completely void of vortices (c).

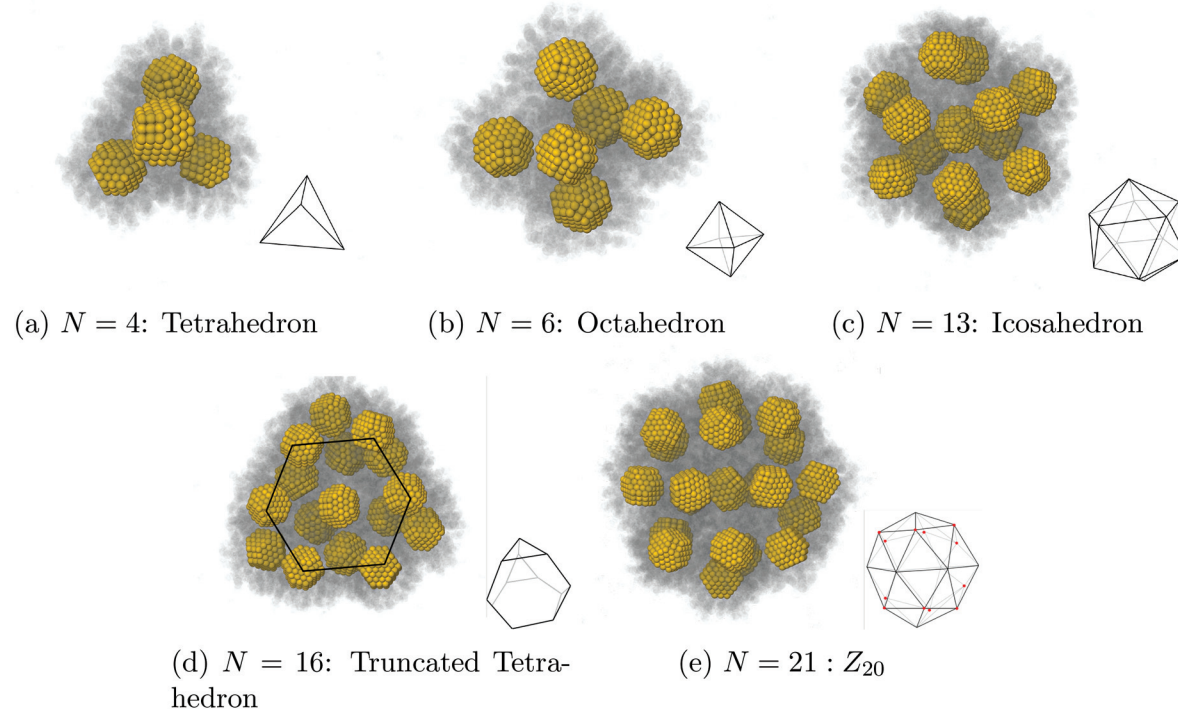


Fig. 9 Summary of equilibrium configurations for our systems. Marked in red on (e) are the locations of the pentamers ($q = +1$ disclinations).

Discussion

Droplet radii

For a pure solvent, the pressure inside the droplet P_l and the vapor pressure P_g satisfy⁴²

$$P_l - P_g = \frac{2\gamma}{R_d}, \quad P_g = P_c e^{\frac{2\gamma v_l}{k_B T R_d}}, \quad (6)$$

where v_l is the molar volume for toluene, reported in ref. 34, P_c the vapor-liquid coexistence pressure, and the surface tension $\gamma \approx 16.5 \text{ mN m}^{-1}$ (ref. 43) at $T = 387$. Note that for $R_d \approx 35 \text{ \AA}$, $\frac{2\gamma v_l}{k_B T R_d} \approx 0.35$, which implies $P_g \approx P_c$ and $P_l \approx 90 \text{ atm}$. Thus, the

very small droplets considered for this study have a high, but not completely unrealistic, pressure.

A formula for the droplet radius as a function of ρ_{avg} , derived in ESI,† is given as:

$$R_d(\rho_{\text{avg}}) = \left(\frac{1 + \frac{4\pi\rho_l N}{3M_w N_t} R_{HS}^3 - \frac{\rho_g}{\rho_{\text{avg}}}}{\frac{4\pi}{3M_w} (\rho_l - \rho_g)} \right)^{1/3} N_t^{1/3} \quad (7)$$

$$= \left(\frac{1 + \frac{N v_{NC}}{N_t v_l} - \frac{\rho_g}{\rho_{\text{avg}}}}{\frac{4\pi}{3M_w} (\rho_l - \rho_g)} t \right)^{1/3} N_t^{1/3} \quad (7)$$



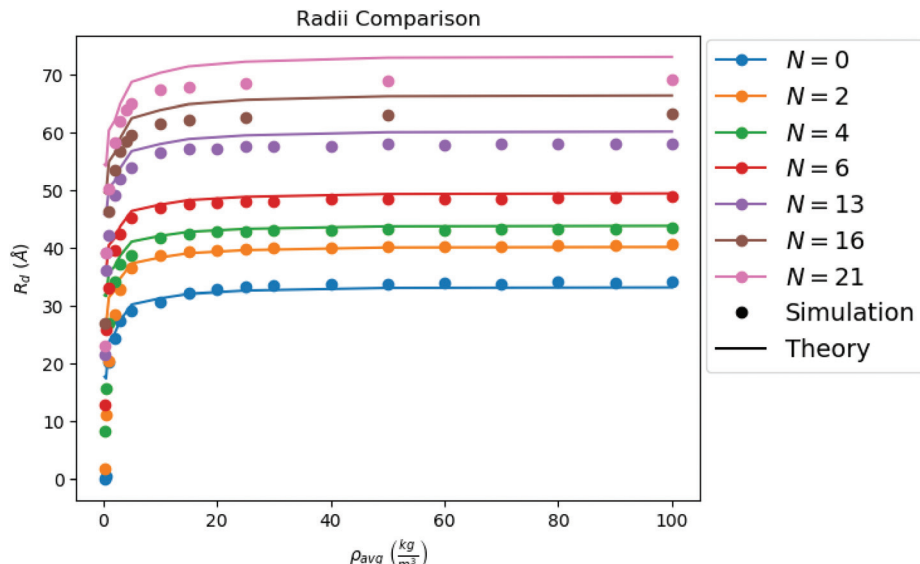


Fig. 10 Comparison between the droplet radii of all of our configurations calculated from simulation, and the droplet radii as predicted by theory (i.e. from eqn (7)).

where R_{HS} is the NC hard sphere radius, defined in eqn (3), v_1 is the equilibrium molar volume of solvent (toluene) in the liquid state and $v_{\text{NC}} = \frac{4\pi}{3}R_{\text{HS}}^3$ is the hard sphere volume of a NC. As shown in Fig. 10, the formula is in excellent agreement with the simulation results, except for a small discrepancy for increasing N , which is discussed in ESI.† The interpretation of the above formula is that, initially, the radius is reduced slowly, but proceeds more efficiently as the first layers are evaporated, as those contain the majority of the solvent molecules.

Relaxation times

The general dependence of R_d on ρ_{avg} , see Fig. 10, is a geometrical relation and does not provide information about the temporal scales associated with the evaporation process. Those are now investigated by computing the relaxation times associated with the latest stages of evaporation ($\rho_{\text{avg}} = 0.25 \text{ kg m}^{-3}$). At a given time, the number of liquid and gas molecules defined from the Gibbs convention, see eqn (S2),† is $N_{\text{liquid}}(t) = N_t - N_{\text{gas}}(t)$. If we assume that there is a single relaxation time τ_R , the evaporation rate follows as:

$$\frac{dN_{\text{gas}}(t)}{dt} = -\frac{1}{\tau_R}N_{\text{liquid}}(t), \quad (8)$$

with solution

$$N_{\text{gas}}(t) = N_t - (N_t - N_{\text{gas}}(0))e^{-t/\tau_R}. \quad (9)$$

According to the classical Maxwell calculation,⁴⁴ evaporation is a diffusion limited process. Hence, the relaxation time involved with a liquid droplet of pure solvent is given by:

$$\tau_R \approx L^2/D^g \quad (10)$$

where $D^g = \frac{2k_B T}{3\pi d_s^2 P_c} \left(\frac{k_B T}{\pi m} \right)^{1/2}$ is the gas diffusion constant and L is the linear size of the box that encloses the gas. At the volume where the toluene liquid droplet evaporates, it is $L \approx 800 \text{ \AA}$, hence:

$$\tau_R(N = 0) \approx 1 \text{ ns}, \quad (11)$$

where the toluene diameter has been taken as $d_s = 4 \text{ \AA}$. There are a number of approximations needed to reach eqn (10) (and eqn (11)) but, as discussed in ref. 44, those are relatively small corrections that do not significantly change the magnitude of τ_R .

The form eqn (9) is in excellent agreement with Fig. 11, providing τ_R as a fitting parameter. We then investigate the dependence of the number N of NCs, where Fig. 12 shows a linear relation:

$$\tau_R = \tau_0 N = 1.312(4)N \text{ ns}. \quad (12)$$

The intercept ($N = 0$) is consistent with zero, which is in agreement with the estimate eqn (11). The relaxation times growing linearly with N reflects the cooperative nature among the solvent molecules trapped into the ligands across the entire structure. It also shows the emergence of a new relaxation time related to the solvent molecules trapped within the NC chains, which is much larger than the Maxwell relaxation time eqn (10).

The plots in Fig. 13 clearly show that the relaxation times dramatically increase in the latest stages of the evaporation process. Initially, they are basically the same as the pure solvent liquid, raising very rapidly at around $\eta_{\text{HS}} \approx \eta_{\text{HS}}^f = 0.49$, the hard sphere freezing transition.⁴⁵

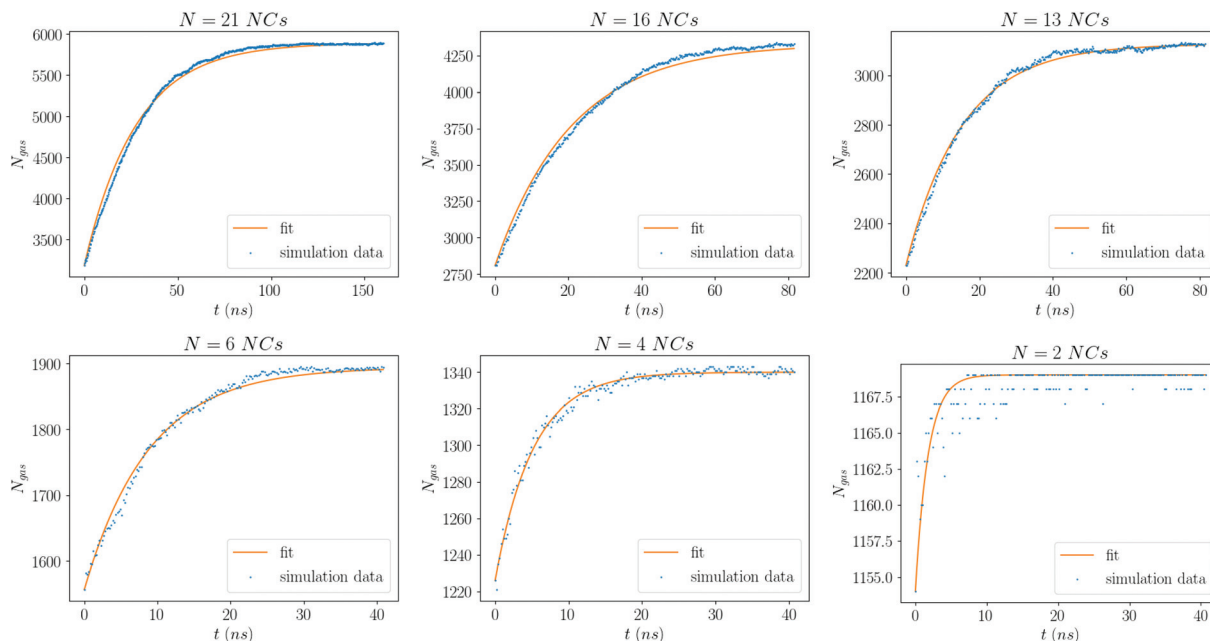


Fig. 11 Number of solvent molecules in the gas phase for each value of N . The curve is a fit to eqn (9). Each plot is for the smallest average density considered, $\rho_{\text{avg}} = 0.25 \text{ kg m}^{-3}$.

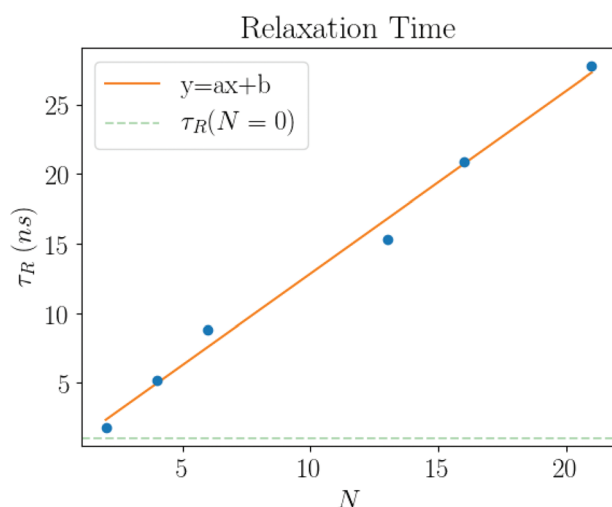


Fig. 12 The relaxation times (τ_R) as a function of number of NCs in the system (N). The fit gives $\tau_0 = 1.312(4) \text{ ns}$, see eqn (12).

Free energy

The free energy of the system is a function of $F(T, \rho_{\text{avg}}, V; N)$. This value may be calculated by integrating the pressure over the volume, see eqn (S11).[†] In the appendix, we derive a relation once the liquid phase disappears:

$$F(T, \rho_{\text{avg}}, V; N) - F(T, \rho_{\text{avg}}, V; N=0) = F_{\text{dry}}(T; N) \quad (13)$$

where $F_{\text{dry}}(T; N)$ is the free energy of a dry system of N NCs with the same structure, which has been calculated

in, for example, ref. 39. The condition of equilibrium implies

$$F_D = -\frac{\partial F_{\text{NC-S}}(T)}{\partial D} = \frac{\partial F_{\text{dry}}(T)}{\partial D} = -F_{\text{D}}^{\text{dry}}, \quad (14)$$

where F_D is the force at distance D between N NCs mediated by the solvent. This equation is of interest as it shows how attractive forces develop as a function of the remaining N_{liquid} molecules. As shown in ESI,[†] the free energy obtained this way is consistent with existing predictions, as quoted in ref. 39, but with much larger error bars.

Conclusions

Solvent evaporation

In this paper, we have presented a description for NC assembly by solvent evaporation, illustrated in Fig. 14. We have considered N NCs contained within a solvent droplet of radius R_d , which is in coexistence with its gas. As evaporation proceeds the droplet shrinks. In the early stages, relaxation times are determined by the liquid/gas coexistence, that is a function of the vapor diffusion constant and independent of the NCs, which are in a liquid-like state themselves, and whose only effect is an increase in the droplet radius, as predicted by eqn (7). Once the hard sphere packing fraction η_{HS} , see eqn (4), reaches the hard sphere freezing point $\eta_{\text{HS}}^f = 0.49$, relaxation times become much longer and adopt a linear dependence on the number of NCs according to:

$$\tau_R = \tau_0 N. \quad (15)$$

The coefficient τ_0 generally depends on the NC and the temperature $P_c(T)$ (or pressure). We should note that even



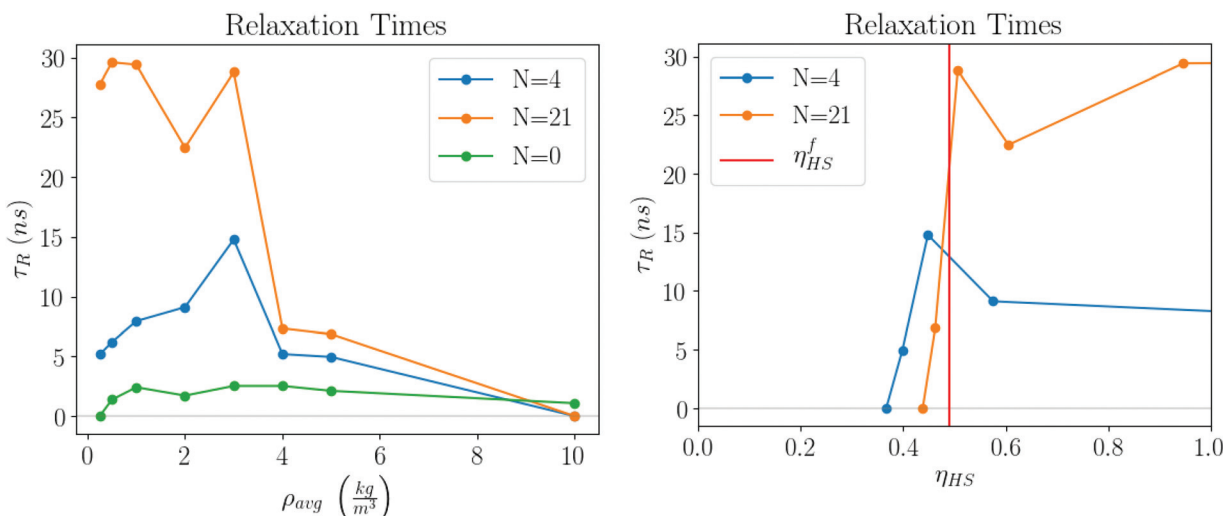


Fig. 13 Relaxation times as the simulation progresses. For $\rho_{avg} > 10$ the values are the same as the pure solvent and are eliminated. On the right, the same data is shown as a function hard sphere packing fraction η_{HS} . A distinct transition is observed near the freezing packing fraction $\eta_{HS}^f = 0.49$.

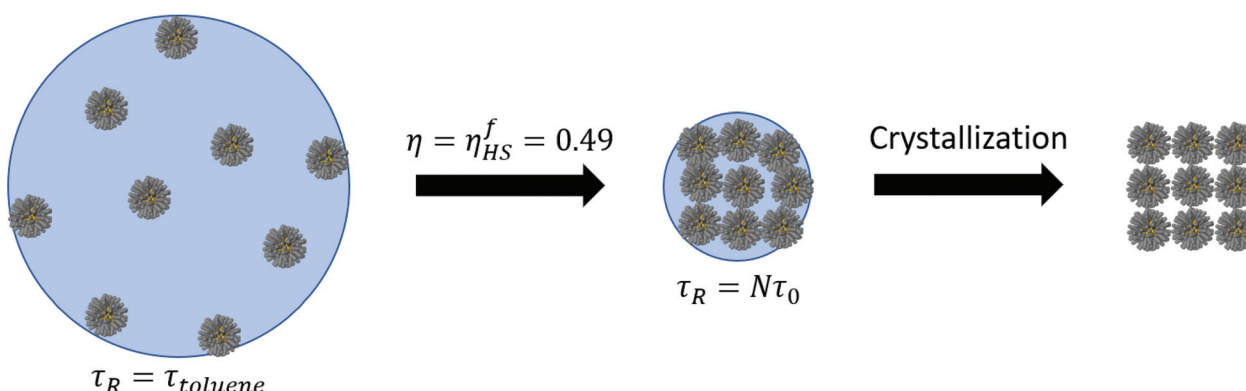


Fig. 14 Illustration of the process of solvent evaporation.

before relaxation times slow down, the liquid-like NCs already hint at what the final structure will be, as shown in Fig. 7b or Fig. 8a, where the distances satisfy the relations for a tetrahedron or icosahedron, even when significant amount of solvent still remains. This point has also been discussed in other contexts.⁴⁶ These results clearly suggest that the slowest relaxation time in the process of assembly by solvent evaporation is not determined by the diffusion constant of the gas but rather, it is dominated by the process of removing the solvent molecules trapped within the ligands.

Certainly, our study has investigated a small number of NCs, but some of our conclusions apply to larger systems. Because the NCs are stable in the liquid droplet (*i.e.* they repel each other in the solvent), the description in terms of hard spheres is plausible and nucleation of fcc/hcp phases may be generally expected for $\eta_{HS} > \eta_{HS}^f$, with a characteristic nucleation time $\tau_N(\eta_{HS})$, which for sufficiently large η_{HS} is always smaller than τ_R . The trapped solvent molecules, however, will need to diffuse through the assembled structure and therefore,

will undergo a random walk through all the N NCs within the system. Thus for large N , eqn (15) is expected to be replaced by:

$$\tau_R \approx \tau'_0 N^{1/2}. \quad (16)$$

where τ'_0 is a new time constant to be determined.

Connection to experiments

Except for the newest experiments of Wang *et al.*¹⁰ and Yang *et al.*,¹¹ all previous BNSLs have been obtained through heterogeneous nucleation, where crystallization occurs on a substrate. Recent experiments have begun to characterize the dynamics of assembly^{14,16} in single component SLs, and establish that the final bcc SL proceeds through an intermediate fcc or hcp phase. In fact, the experiments in ref. 16 report a hcp to bcc transition at around $\eta_{HS} \approx 0.6$, in agreement with the qualitative arguments provided above, even though there is evidence for the hcp phase at $\eta_{HS} \approx 0.4 < \eta_{HS}^f = 0.49$, in slight disagreement with our predictions. It would be of great interest if

experiments in homogeneous nucleation could establish the presence of this intermediate phase.

We note that both fcc and hcp are built from tetrahedral and octahedral units, the very same building blocks defining the equilibrium structures found in this study. SLs formed from tetrahedral and octahedral elements (Quasi Frank-Kasper phases) encompass all known experimental examples of BNSLs.⁴¹ Recent imaging techniques may be able to visualize the assembly of clusters and validate the predictions in this paper.^{13,47}

Controlling the quality of the structures

Our study suggests that the evaporation rate does not play any role during the assembly process provided that $\eta_{\text{HS}} < \eta_{\text{HS}}^f$. Thus, in order to accelerate synthesis, the first step of evaporating the “free” (not trapped within the ligands) liquid solvent may proceed arbitrarily fast. It is after this point that relaxation times dramatically increase, and the evaporation rate must keep pace with the system relaxation times, as predicted by eqn (12).

The important parameter controlling the quality of the assembled structures is the Pe number, eqn (1). Rather unexpectedly, recent results²¹ for Lennard-Jones particles have shown that the quality of the crystal is insensitive to the Pe number over a significant region. With the diffusion constant given from:

$$D_{\text{NC}} = \frac{k_{\text{B}}T}{6\pi\eta_{\text{t}}R_{\text{HS}}}, \quad (17)$$

where R_{HS} has been defined in eqn (3) and η_{t} is the viscosity of the solvent, all these considerations are directly applicable. However, as discussed extensively, the rapid rise of relaxation times due to the effect of the capping ligand chains as a function of N modifies some of the predictions obtained with coarse-grained models. Further applications to actual experiments will help clarify this point.

Outlook

In summary, our paper has provided a detailed microscopic description of assembly by solvent evaporation. There are many quantitative aspects that will need to be subject of further investigation, namely, the dependence of relaxation times on the temperature and NC type, and investigation of larger assemblies and other type of solvents. It is our expectation to fill these gaps in the near future.

Materials and methods

We have run molecular dynamics simulations of the above numbers of nanocrystals using the HOODLT³⁰ and HOOMD-blue software package⁴⁸ using a Langevin integrator at a temperature $T = 387$ K with time step $dt = 0.0267$ and non-bonded cutoff of 24 Å. Simulations used the OPLS/united force field²⁹

Table 1 The corresponding numbers of nanocrystals (N) and toluene molecules (N_{t})

N	N_{t}
0	800
2	1169
4	1343
6	1896
13	3145
16	4405
21	5924

as implemented in HOODLT.³⁰ The parameters for toluene were obtained from Ref. 31. Simulations were carried out in the following manner:

N NCs were placed along with N_{t} toluene molecules (see Table 1) in a cubic box of length l_0 , such that the average density of the solvent in the box was $\rho_{\text{avg}} = 100 \text{ kg m}^{-3}$. Then the simulation began and the system was allowed to run for 10^6 time steps. Then, over the next 10^5 time steps, the simulation box was expanded to a new length $l_1 > l_0$ and we again ran the simulation while collecting data for 10^6 time steps. This process of running the simulation, lengthening the simulation box, and running the simulation at a new average density was repeated many times until the solvent was completely evaporated. We refer to each iteration of this process as a window. Typically, there were 12–23 windows in a completed simulation. After initial runs in each window, more statistics for each window were obtained from runs of 10^7 or more time steps individually on the XSEDE Comet GPU Cluster.

Conflicts of interest

There are no conflicts to declare.

Acknowledgements

A. T. acknowledges many discussions and clarification of their work with I. Coropceanu, B. Patra and D. Talapin. Interest and discussions are also acknowledged from L. Liz-Marzan, S. Mallapragada and D. Vaknin. The work is funded by NSF, DMR-CMMT 1606336 “CDS&E: Design Principles for Ordering Nanoparticles into Super-crystals”. This work used the Extreme Science and Engineering Discovery Environment (XSEDE), which is supported by National Science Foundation grant number ACI-1548562. Our project within XSEDE is supported by grant TG-MCB140071.

References

- 1 M. A. Boles, M. Engel and D. V. Talapin, Self-Assembly of Colloidal Nanocrystals: From Intricate Structures to Functional Materials, *Chem. Rev.*, 2016, **116**, 11220–11289.



2 D. Nykypanchuk, M. M. Maye, D. van der Lelie and O. Gang, DNA-guided crystallization of colloidal nanoparticles, *Nature*, 2008, **451**, 549–552.

3 S. Y. Park, A. K. R. Lytton-Jean, B. Lee, S. Weigand, G. C. Schatz and C. A. Mirkin, DNA-programmable nanoparticle crystallization, *Nature*, 2008, **451**, 553–556.

4 E. Auyeung, T. I. N. G. Li, A. J. Senesi, A. L. Schmucker, B. C. Pals, M. O. de la Cruz and C. A. Mirkin, DNA-mediated nanoparticle crystallization into Wulff polyhedra, *Nature*, 2014, **505**, 73–77.

5 H. Zhang, W. Wang, S. Mallapragada, A. Travesset and D. Vaknin, Macroscopic and tunable nanoparticle superlattices, *Nanoscale*, 2017, **9**, 164–171.

6 S. Nayak, N. Horst, H. Zhang, W. Wang, S. Mallapragada, A. Travesset and D. Vaknin, Interpolymer Complexation as a Strategy for Nanoparticle Assembly and Crystallization, *J. Phys. Chem. C*, 2019, **123**, 836–840.

7 R. L. Whetten, M. N. Shafiqullin, J. T. Khouri, T. G. Schaaff, I. Vezmar, M. M. Alvarez and A. Wilkinson, Crystal Structures of Molecular Gold Nanocrystal Arrays, *Acc. Chem. Res.*, 1999, **32**, 397–406.

8 E. V. Shevchenko, D. V. Talapin, N. A. Kotov, S. O'Brien and C. B. Murray, Structural diversity in binary nanoparticle superlattices, *Nature*, 2006, **439**, 55–59.

9 M. A. Boles and D. V. Talapin, Many-Body Effects in Nanocrystal Superlattices: Departure from Sphere Packing Explains Stability of Binary Phases, *J. Am. Chem. Soc.*, 2015, **137**, 4494–4502.

10 P.-p. P. Wang, Q. Qiao, Y. Zhu and M. Ouyang, Colloidal Binary Supracrystals with Tunable Structural Lattices, *J. Am. Chem. Soc.*, 2018, **140**, 9095–9098.

11 Y. Yang, B. Wang, X. Shen, L. Yao, L. Wang, X. Chen, S. Xie, T. Li, J. Hu, D. Yang and A. Dong, Scalable Assembly of Crystalline Binary Nanocrystal Superparticles and Their Enhanced Magnetic and Electrochemical Properties, *J. Am. Chem. Soc.*, 2018, **140**, 15038–15047.

12 A. Sánchez-Iglesias, M. Grzelczak, T. Altantzis, B. Goris, J. Pérez-Juste, S. Bals, G. Van Tendeloo, S. H. Donaldson, B. F. Chmelka, J. N. Israelachvili and L. M. Liz-Marzán, Hydrophobic interactions modulate self-assembly of nanoparticles, *ACS Nano*, 2012, **6**, 11059–11065.

13 S. Merkens, M. Vakili, A. Sanchez-Iglesias, L. Litti, Y. Gao, P. V. Gwozdz, L. Sharpnack, R. H. Blick, L. M. Liz-Marzan, M. Grzelczak and M. Trebbin, Time-Resolved Analysis of the Structural Dynamics of Assembling Gold Nanoparticles, *ACS Nano*, 2019, **13**, 6596–6604.

14 M. C. Weidman, D.-M. M. Smilgies and W. A. Tisdale, Kinetics of the self-assembly of nanocrystal superlattices measured by real-time in situ X-ray scattering, *Nat. Mater.*, 2016, **15**, 775–781.

15 Z. Fan and M. Grünwald, *Orientational Order in Self-Assembled Nanocrystal Superlattices*, 2019, <https://pubs.acs.org/sharingguidelines>.

16 I. Lokteva, M. Koof, M. Walther, G. Grübel and F. Lehmkühler, Monitoring Nanocrystal Self-Assembly in Real Time Using In Situ Small-Angle X-Ray Scattering, *Small*, 2019, **15**, 1900438.

17 M. Wang and J. F. Brady, Microstructures and mechanics in the colloidal film drying process, *Soft Matter*, 2017, **13**, 8156–8170.

18 M. P. Howard, A. Nikoubashman and A. Z. Panagiotopoulos, Stratification Dynamics in Drying Colloidal Mixtures, *Langmuir*, 2017, **33**, 3685–3693.

19 S. Cheng and G. S. Grest, Structure and diffusion of nanoparticle monolayers floating at liquid/vapor interfaces: A molecular dynamics study, *J. Chem. Phys.*, 2012, **136**, 214702.

20 S. Cheng and G. S. Grest, Molecular dynamics simulations of evaporation-induced nanoparticle assembly, *J. Chem. Phys.*, 2013, **138**, 64701.

21 M. P. Howard, W. F. Reinhart, T. Sanyal, M. S. Shell, A. Nikoubashman and A. Z. Panagiotopoulos, Evaporation-induced assembly of colloidal crystals, *J. Chem. Phys.*, 2018, **149**, 094901.

22 A. F. Routh and W. B. Zimmerman, Distribution of particles during solvent evaporation from films, *Chem. Eng. Sci.*, 2004, **59**, 2961–2968.

23 A. Travesset, Binary nanoparticle superlattices of soft-particle systems, *Proc. Natl. Acad. Sci. U. S. A.*, 2015, **112**, 9563–9567.

24 N. Horst and A. Travesset, Prediction of binary nanoparticle superlattices from soft potentials, *J. Chem. Phys.*, 2016, **144**, 014502.

25 A. Travesset, Nanoparticle Superlattices as Quasi-Frank-Kasper Phases, *Phys. Rev. Lett.*, 2017, **119**, 1–5.

26 A. Travesset, Soft Skyrmions, Spontaneous Valence and Selection Rules in Nanoparticle Superlattices, *ACS Nano*, 2017, **11**, 5375–5382.

27 J. A. Anderson, C. D. Lorenz and A. Travesset, Micellar crystals in solution from molecular dynamics simulations, *J. Chem. Phys.*, 2008, **128**, 184906.

28 T. D. Nguyen, C. L. Phillips, J. A. Anderson and S. C. Glotzer, Rigid body constraints realized in massively-parallel molecular dynamics on graphics processing units, *Comput. Phys. Commun.*, 2011, **182**, 2307–2313.

29 W. L. Jorgensen, J. D. Madura and C. J. Swenson, Optimized intermolecular potential functions for liquid hydrocarbons, *J. Am. Chem. Soc.*, 1984, **106**, 6638–6646.

30 A. Travesset, Phase diagram of power law and Lennard-Jones systems: Crystal phases, *J. Chem. Phys.*, 2014, **141**, 164501.

31 C. D. Wick, M. G. Martin and J. I. Siepmann, Transferable Potentials for Phase Equilibria. 4. United-Atom Description of Linear and Branched Alkenes and Alkylbenzenes, *J. Phys. Chem. B*, 2000, **104**, 8008–8016.

32 J. T. Fern, D. J. Keffer and W. V. Steele, Vapor?Liquid Equilibrium of Ethanol by Molecular Dynamics Simulation and Voronoi Tessellation, *J. Phys. Chem. B*, 2007, **111**, 13278–13286.

33 J. T. Fern, D. J. Keffer and W. V. Steele, Measuring Coexisting Densities from a Two-Phase Molecular



Dynamics Simulation by Voronoi Tessellations, *J. Phys. Chem. B*, 2007, **111**, 3469–3475.

34 R. D. Goodwin, Toluene Thermophysical Properties from 178 to 800 K at Pressures to 1000 Bar, *J. Phys. Chem. Ref. Data*, 1989, **18**, 1565–1636.

35 U. Landman and W. D. Luedtke, Small is different: energetic, structural, thermal, and mechanical properties of passivated nanocluster assemblies, *Faraday Discuss.*, 2004, **125**, 1–22.

36 X. Zha and A. Travesset, Stability and Free Energy of Nanocrystal Chains and Superlattices, *J. Phys. Chem. C*, 2018, **122**, 23153–23164.

37 C. Waltmann, N. Horst and A. Travesset, Capping Ligand Vortices as “atomic Orbitals” in Nanocrystal Self-Assembly, *ACS Nano*, 2017, **11**, 11273–11282.

38 C. Waltmann, N. Horst and A. Travesset, Potential of mean force for two nanocrystals: Core geometry and size, hydrocarbon unsaturation, and universality with respect to the force field, *J. Chem. Phys.*, 2018, **149**, 034109.

39 T. Waltmann, C. Waltmann, N. Horst and A. Travesset, Many Body Effects and Icosahedral Order in Superlattice Self-Assembly, *J. Am. Chem. Soc.*, 2018, **140**, 8236–8245.

40 A. Haji-Akbari and S. C. Glotzer, Strong orientational coordinates and orientational order parameters for symmetric objects, *J. Phys. A: Math. Theor.*, 2015, **48**, 485201.

41 A. Travesset, Topological structure prediction in binary nanoparticle superlattices, *Soft Matter*, 2017, **13**, 147–157.

42 P. G. Debenedetti, *Metastable Liquids Concepts and Principles*, Princeton University, 1996.

43 C. Wohlfarth and C. Wohlfarth, *Surface Tension of Pure Liquids and Binary Liquid Mixtures*, Springer Berlin Heidelberg, Berlin, Heidelberg, 2019, pp. 144–144.

44 N. Fuchs, *Evaporation and Droplet Growth In Gaseous Media*, Pergamon Press, I edn., 1959, pp. 1–72.

45 D. Frenkel and B. Smit, *Understanding Molecular Simulation*, Academic Press, San Diego, 2nd edn., 2002, p. 638.

46 P. F. Damasceno, M. Engel and S. C. Glotzer, Predictive Self-Assembly of Polyhedra into Complex Structures, *Science*, 2012, **337**, 453–457.

47 J. E. Galván-Moya, T. Altantzis, K. Nelissen, F. M. Peeters, M. Grzelczak, L. M. Liz-Marzán, S. Bals and G. Van Tendeloo, Self-organization of highly symmetric nanoassemblies: A matter of competition, *ACS Nano*, 2014, **8**, 3869–3875.

48 J. A. Anderson, C. D. Lorenz and A. Travesset, General purpose molecular dynamics simulations fully implemented on graphics processing units, *J. Comput. Phys.*, 2008, **227**, 5342–5359.

